This manuscript is a preprint that has been submitted but not been accepted for publication. Subsequent versions of this manuscript may have different content. If accepted, the final version of this manuscript will be available via the ‘Peer-reviewed Publication DOI’ link on the right-hand side of this webpage. Please feel free to contact the authors. We welcome feedback.

Stress perturbations from hydrological and industrial loads and seismicity in the Salt Lake City region

Xie Hu[1], Liang Xue[2], Roland Bürgmann[1], Yuning Fu[2], Teng Wang[3]

[1] Department of Earth and Planetary Science and Berkeley Seismological Laboratory, University of California Berkeley, Berkeley, CA, USA

[2] School of Earth, Environment and Society, Bowling Green State University, Bowling Green, OH, USA

[3] School of Earth and Space Sciences, Peking University, Beijing, China

Key Points:

- The M5.7 Magna earthquake, its aftershocks and persistent microseismicity cluster next to a mine tailings impoundment
- The elastic stress produced by industrial loads exceeds that from hydrological sources by two orders of magnitude in the hypocentral zone
- Aggregate tailings yield stressing rates comparable to tectonic loading and could delay or hasten nearby ruptures by hundreds of years

Abstract: The March 18, 2020 M5.7 Magna earthquake awakened people from decades of seismic quiescence in Salt Lake City, Utah. The event occurred just east of a mine tailings impoundment that receives ~60 million tons/yr of ore waste products since the early 1900s. Here we investigate elastic loading effects due to the anthropogenic mass transfer and various natural hydrological loads. We note a possible spatial correlation between earthquake clusters and Coulomb stress changes of tens of kPa due to the tailings loads. In contrast, long-term and seasonal stress changes from hydrological loads are only several kPa. A lack of statistically significant seasonality in seismicity suggests a weak control by cyclic hydrological loads. Anthropogenic loading rates of ~ 1 kPa/yr at seismogenic depths during recent decades may accelerate or decelerate event occurrences by several hundreds of years, mainly depending on the encompassing fault geometries.

Plain Language Abstract: The interconnection between anthropogenic surface modifications and natural hazards has received relatively little attention due to their small dimensions and shallow locations. We note a compelling spatial correlation between a mine tailings impoundment and the March 18, 2020 M5.7 Magna earthquake, its aftershocks, and persistent earthquake clusters in the Salt Lake City region. This highly populated region hosts various industrial, hydrological, and tectonic processes, including the world's largest man-made excavation, the Bingham Canyon mine, and its associated tailings facility, the Great Salt Lake and Utah Lake, a dynamic aquifer system, regional soil moisture and snow loads, as well as the seismically active Wasatch Fault Zone. Here we characterize the spatio-temporal stress changes since the early 1900s due to the industrial and hydrological sources. The lack of statistically significant seasonality in seismicity suggests a weak correlation with the cyclic hydrological loads. On the other hand, the aggregate tailings load may accelerate or decelerate the seismicity by hundreds of years depending on the location, geometry and frictional properties of active faults. Comprehensive seismic monitoring near sites of industrial production is warranted in fragile geological and tectonic settings to ensure socioeconomic health and sustainable development.

Keywords: 2020 Magna earthquake; mine tailings impoundment; hydrological loads; Coulomb stress; seismicity; anthropogenic impact

1. Introduction

The complex nature of earthquakes and other geohazards has taught us that failure mechanisms in the crust rarely occur in isolation. Tectonic, hydroclimatic and anthropogenic factors may influence eventual catastrophic failure. Changes in surface mass loads and subsurface pore pressure, such as from reservoir impoundment (e.g., Talwani, 1997; Gupta, 2002; Ge et al., 2009), open-pit and underground mining (e.g., Pankow et al., 2014; Li et al., 2007), extreme climate (e.g., Costain & Bloolinger, 2010) and fluid injection and withdrawal (e.g., González et al., 2012; Ellsworth, 2013; Rubinstein and Mahani, 2015; Wetzler et al., 2019), may perturb the subsurface stress field, making critically stressed seismogenic zones more vulnerable. In particular, regional hydrological loading has been recognized to modulate seismicity, often exhibited in an annual period in the number of earthquakes, such as in Himalayas (Bettinelli et al., 2008), California (Amos et al., 2014; Johnson et al., 2017), the New Madrid Seismic Zone (Craig et al., 2017), southern Alaska (Johnson et al., 2020), and the East African Rift System (Xue et al., 2020). However, artificial load changes from landfills, construction, or quarrying may also induce dynamic failures (e.g., Qian et al., 2019; Ampuero et al., 2020), yet have been largely neglected due to their small dimensions and shallow locations.

Salt Lake City (SLC) and the nearby Great Salt Lake are located in the hanging wall of the Wasatch Fault Zone (WFZ), forming the eastern margin of the Basin and Range province (Fig. 1). The ~40-km SLC segment along the central WFZ has a vertical slip rate between 0.9 and 1.8 mm/yr, a recurrence interval of surface-breaking ruptures of 1,300-1,500 yr, and the latest surface-rupturing event dates back to 1,300±200 yr B.P. (DuRoss and Hylland, 2015; DuRoss et al., 2016). The basin also hosts the east-dipping West Valley Fault Zone (WVFZ) to the west of the Jordan River, and subparallel to the WFZ, constituting a graben that hosts a dynamic confined aquifer (Hu et al., 2018; Hu & Bürgmann, 2020). To the south, the Traverse Mountains separate the Salt Lake basin from another remnant of prehistoric Lake Bonneville, the Utah Lake.

Of particular significance to the local economy and history, the Bingham mining district in the Oquirrh Mountains west of the Salt Lake basin has supported generations of SLC residents since its initial discovery around 1850 (Krahulec, 2018). It features the world's largest man-made excavation and open-pit ore mine – the Bingham Canyon mine (e.g., Krahulec, 2018). The open-pit mining operation officially started in 1906 and the tailings have been transported ~20 km north and deposited in an impoundment to the north of Magna, adjacent to the south shore of Great Salt Lake. The recent M5.7 Magna earthquake struck the metropolitan SLC region on March 18th, 2020. Intriguingly, the M5.7 event and its aftershocks occurred immediately east of the tailings dam, where historical microseismicity has also been clustered for many decades (Figs. 2 and S2) (Bowman & Arabasz, 2017; Hu et al., 2017; Hu & Bürgmann, 2020).

To address concerns about the potential impact of natural and anthropogenic load changes on seismic hazards, especially near dense population centers, we investigate the potential spatio-temporal correlations between the elastic stress changes induced by hydrological and industrial loads and the distribution of earthquakes in the SLC region since 1900 (Fig. S1). We find that while seasonal and long-term stress changes from hydrological loads (lakes, aquifers, soil moisture, and snow) are small and do not appear to modulate seismicity in this area, more than one century of mining tailings accumulation from the Bingham Mine substantially modified the local stress (tens of kPa) at the hypocenter of the 2020 Magna earthquake and nearby clusters of historic seismicity and could have delayed or hastened event occurrences by a few hundred years.

Fig. 1

2. Data and Methods

2.1. Earthquake Catalogs

University of Utah Seismograph Stations (UUSS) archives one historical, two pre-digital, and one modern earthquake catalog for the Utah region (Lat. 36.75° to 42.50° N, Long. 108.75° to 114.25° W) (Figs. 3 and S2-S5; Table S1).

For the 2020 Magna earthquake sequence, a total of 2017 events were detected after the mainshock in the period from March 18 to May 6, 2020 (Fig. 2). The spatial distribution of the aftershock sequence shows two distinct clusters that we refer to as cluster *W* and cluster *E*. Similar to the distribution of microseismicity since 1980 in the modern catalog (Hu & Bürgmann, 2020), cluster *W* produced more events and lies at a greater depth than cluster *E* (Fig. S6).

The earthquake catalogs compiled by UUSS recorded more than 20 earthquakes with M>3 surrounding the tailings impoundment during 1900-2018 (Figs. 4b and S7). The largest pre-2020 earthquake in cluster *W* was a M5.2 event at a focal depth of ~10.7 km on September 5, 1962 (Wong et al., 1995). Wong et al. (1995) proposed that a ~20-km-long, buried and east-dipping "Saltair structure" represents the source fault of the 1962 event, based on the distribution of a small number of aftershocks and gravity anomaly. The latest aftershock relocations of the 2020 Magna earthquake by UUSS do support seismicity on planes dipping steeply to the east (Pang et al., 2020; UUSS, 2020a). The east-dipping WVFZ lies just west of cluster *E* and may have jointly produced both long-term and aftershock activity in that shallow zone (Fig. 2).

Fig. 2

2.2. Mine and Tailings Impoundment

The Oquirrh Mountains host the Bingham Canyon copper mine that started its production in the early 1900s (Hu et al., 2017, and references therein). A ~34-km^2 tailings impoundment was developed just south of the Great Salt Lake, consisting of a 20-km^2, now inactive south pond close to the residential area of Magna and a 14-km^2 north pond holding the tailings since ~2001. In recent years, about 60 million tons of tailings are deposited in the impoundment per annum (Rio Tinto, 2019). We consider the time series of annual production of raw ore from 1904-05 to 2017 (Fig. S7) as the cumulative tailings load, as only a small fraction of the material is refined into copper and other precious metals (Krahulec, 2018). We assume that the amount of mass reduction at the mine site is the same as the mass increase at the tailings pond.

2.3. Surface loading from Great Salt Lake and Utah Lake

The prehistoric Lake Bonneville was the largest of numerous late Pleistocene pluvial lakes in the region reaching a maximum depth of 380 m and an area of 52,000 km^2 (Gilbert, 1890). As a consequence of abrupt postglacial unloading and associated viscoelastic rebound (Bills et al., 1994), a faster slip rate and increased seismicity over the Wasatch region has been inferred from time-dependent stress modeling, Holocene to recent geologic, palaeoseismological, and geodetic data (Hetzel & Hampel, 2005).

We obtain the water level record of the Great Salt Lake (1847 to present) and the Utah Lake (2012 to present) (Fig. S7). The lake levels vary seasonally, reaching their maxima around May due to abundant recharge from mountain snowmelt. The lake levels also vary over multi-year time scales due to climate variability, including substantial lake drawdowns from the late 1980s to early 1990s, from the late 1990s to early 2000s, and most recently from 2012 to 2016.

2.4. Loading from Soil Moisture, Snow and Aquifer Water Equivalent Thickness Changes

The seasonal changes in water equivalent thickness from soil moisture (North American Land Data Assimilation System (NLDAS) Noah model; Mitchell et al., 2004) and snowfall (SNOw Data Assimilation System (SNODAS); NOHRSC, 2004; Argus et al., 2014) are each up to ~0.5 m (Fig. S8). A dynamic aquifer in the graben between the WVFZ and WFZ is characterized by cyclic seasonal discharge/recharge processes (Hu et al., 2017). From the first-order correlation between the seasonal groundwater level changes and the poroelastic displacements of the aquifer skeleton, Hu & Bürgmann (2020) estimated a water equivalent thickness change of less than one meter and a corresponding seasonal volume change of 0.03-0.06 km^3 (Fig. 4d), which allows us to further explore the seasonal loading effect from this local hydrological unit.

2.5. Loading Model and Stress Computation

To fully characterize both the natural and anthropogenic loading effects on the SLC region, we consider hydrological loads from the Great Salt Lake, Utah Lake, snow, soil moisture, and a local aquifer, as well as the artificial counterpart from the tailings deposits. We compute their respective contributions to subsurface stress changes and spatio-temporal variations at both multi-annual and seasonal scales. The stress distributions from snow and soil moisture represent regional effects dominated by seasonal variations, and the aquifer load also does not exhibit appreciable multi-annual changes (Hu and Bürgmann, 2020). Therefore, we only focus on their seasonal variations. We apply a finite-element model to compute the stress fields using the software PyLith

(Aagaard et al., 2013). We use an elastic Earth structure constrained by the seismic velocities defined in the WUS model (Herrmann et al., 2011; Whidden and Pankow; 2012) and the densities from the global PREM (Dziewonski and Anderson, 1981).

Since the M5.7 and its aftershocks occurred in a complicated seismogenic regime with west- and east-dipping structures, we consider a west-dipping scenario with striking 182º and dipping 29º (linear fit through the relocated aftershocks from March 18 through March 24 in cluster *W*; Pang et al., 2020; UUSS, 2020b), and an east-dipping scenario with striking 320º and dipping 65º (based on the east-dipping nodal planes of the M5.7 and large aftershocks reported by USGS) for the stress computations. We use an effective friction coefficient of 0.4 to compute the Coulomb stress change assuming pure normal faulting.

3. Results

To compare the Coulomb stress changes $\Delta\sigma_c$ due to different long-term loading sources, we first focus on a ~45-km-long EW cross section (white line in Fig. 1) (e.g., Figs. 3a-f). We also extract 2D horizontal map views of stress changes at a depth of 9 km (e.g., Figs. 3g-l).

3.1 Historic Coulomb Stress Changes

The long-term decrease of the Great Salt Lake load from 1900 to 2020 by ~3 m (Fig. 4c) unclamps the fault and results in a net increase of $\Delta\sigma_c$ by ~3 kPa for the 29º west-dipping geometry and by ~0.4 kPa for the 65º east-dipping geometry in the hypocentral zone (Figs. 4a, d, g, j). Though small in dimensions compared to the Great Salt Lake, the ore transport from the mine 20-km north to the tailings pond from 1905 to 2017, generated more than one hundred kPa of Coulomb stress changes in the upper few km and tens of kPa at 9 km depth (Figs. 4b, e, h, k), two orders of magnitude larger than the hydrological sources. The changes in Coulomb stresses are opposite in the seismogenic zone for the west and east dipping scenarios, as a result of the competing effects of normal and shear stresses (Figs. S10-S11). Specifically, the ore deposition results in a $\Delta\sigma_c$ decrease by ~45 kPa in cluster *W* for the west-dipping geometry and a $\Delta\sigma_c$ increase by ~45 kPa for the steeply east-dipping geometry. Supplementary figure S12 summarizes the sensitivity of the modeled stresses from the tailings load to the strike and dip angles. Various combinations of east or west dipping strike and dip can yield positive $\Delta\sigma_c$ at the M5.7 hypocenter.

Fig. 3

3.2. Seasonal Coulomb Stress Changes

Hydrological loading has been well documented in modulating the stress field and seismicity in tectonically active regions, especially following cyclic behaviors with distinct seasons. During the wet season, the shallow aquifer (160 km^2 in area and 600 m in depth) contributes to a decreased $\Delta\sigma_c$ to its east and an increased $\Delta\sigma_c$ to its west with a peak amplitude of ~0.5 kPa at seismogenic depths for both considered fault geometries (Figs. 3i, l), and an opposite $\Delta\sigma_c$ occurs during the dry summer and fall. Cluster *W*, which is ~10 km northwest of and ~10 km below the shallow aquifer, encounters negligible $\Delta\sigma_c$. Cluster *E* is closer to the aquifer and experiences ~0.3 and ~0.1 kPa changes in $\Delta\sigma_c$ for west- (Fig. 3c) and east-dipping (Fig. 3f) scenarios, respectively. We also consider the elastic loading sources from the Great Salt Lake, Utah Lake, soil moisture, and snow water for a one-year period (i.e., 3/2019-2/2020), and compute $\Delta\sigma_c$ at the M5.7 hypocenter for the west-dipping geometry (Fig. 4a). The elastic loads from the Great Salt Lake and Utah Lake present similar phases in Coulomb stress with a peak in September when the seasonal load is at a minimum. Decrease in soil moisture and near absence of snow cover during July to October introduces months of low Coulomb stress in the hypocenter zone.

4. Discussion

4.1 Seasonal Stress Modulations

The hydrological sources only produce a net peak-to-peak seasonal amplitude of 0.44 kPa for the shallow west-dipping fault at the M5.7 hypocenter (Fig. 4a). The east-dipping scenario results in a net seasonal stress change of 0.24 kPa (Fig. S13). For comparison, in California the periodic non-tectonic hydroclimatic sources contribute to a seasonal $\Delta\sigma_c$ in the range of 0.5 to 2 kPa on the fault systems adjacent to the Sierra Nevada, which may increase the seismicity by 10% when aligned with the background stress (Johnson et al., 2017). Here, due to the low number of detected events we find no clear evidence of seasonal variation in seismicity in the SLC region including clusters *W* and *E* (Figs. S2-S5) (Hu & Bürgmann, 2020).

Fig. 4

4.2. Long-term Stress Perturbations

For a more quantitative comparison, we focus on a long-term time frame from 1900 when the data of both the ore mass and Great Salt Lake level changes are available. The Great Salt Lake levels have fluctuated on a multi-annual timescale in response to the prolonged extreme climates yet the consequent $\Delta\sigma_c$ near the Magna earthquake hypocenter are modest (±4 kPa). The $\Delta\sigma_c$ rate can occasionally reach ±0.9 kPa/yr for the west-dipping scenario (orange lines in Figs. 4 b and c), while the $\Delta\sigma_c$ and its rate are only ±0.5 kPa and ±0.1 kPa/yr for the east-dipping scenario (orange lines in Figs. S13 b and c).

Unlike the cyclic loading and unloading from the hydrosphere, the tailings structures underwent a cumulative increase in load (Krahulec, 2018). By the latest reported record in 2017, $\Delta\sigma_c$ from the tailings decreased by 45 kPa assuming the west-dipping geometry, and the rate of $\Delta\sigma_c$ increased to -0.8 kPa/yr for most years after 1990 (blue lines in Fig. 4b). In contrast, for the east-dipping geometry the increase of $\Delta\sigma_c$ and its rate amount to 45 kPa and 0.8 kPa/yr (Fig. S13). The anthropogenic stress and stressing rate changes can be compared with the background tectonic loading rates from physical models as well as from earthquake stress drops and recurrence intervals.

The tectonic loading rate of the WFZ was estimated at a few to a dozen of kilopascal per year. Bagge et al. (2019) relied on a 3D finite-element model to resolve the interseismic stress increase due to the eastern Basin-Range extension at ∼19 kPa/yr on the central WFZ and ∼12-14 kPa/yr on the WVFZ. Verdecchia et al. (2019) used a dislocation model to estimate a stressing rate of ~3.6 kPa/yr at 13-km and ~2.3 kPa/yr at 12-km depth. A simple back-of-the-envelope estimate considers a typical stress drop of 1-10 MPa per 1300-year recurrence interval on the SLC segment of the WFZ, suggesting a tectonic stressing rate of 0.77-7.7 kPa/year.

The tailings-induced $\Delta\sigma_c$ rate has been maintained at about -0.8 kPa/yr (west dip) or 0.8 kPa/yr (east dip) for about the last three decades. Overall, the tailings load can generate comparable elastic stress changes to those from tectonic loading.

4.3. Linking Loads to Seismicity

Depending on the receiver fault geometry and effective coefficient of friction, the stress distribution due to the ore deposition at the tailings pond can be partially correlated with the location of the M5.7 earthquake sequence and the long existing local seismicity cluster *W* (Fig. 3). High-angle normal faults at the Wasatch front appear to shallow into a listric geometry at a depth of 8-12 km as revealed by seismic reflection profiling (e.g., Velasco et al., 2010). The M5.7 earthquake is considered to have ruptured a patch on the deep listric portion of the WFZ dipping to the west (e.g., Pang et al., 2020; UUSS, 2020a; 2020b). However, we cannot rule out the role of east-dipping seismogenic structures hosting some of the aftershocks of the M5.7 and long-standing small earthquakes. The east-dipping Saltair structure was inferred from the distribution of aftershocks of the 1962 event and a gravity low around cluster *W* (Wong et al., 1995). The latest aftershock relocations by UUSS also support planes dipping to the east (Pang et al., 2020). Our results suggest a possible role of the cumulative ore deposition in producing enduring spatial concentrations of microseismicity. For either nodal planes observed in M5.7 and big aftershocks, the principal earthquake cluster *W* falls in the marginal zone of the $\Delta\sigma_c$ decrease (west-dipping scenario) or increase (east-dipping scenario) by tens of kPa, and the $\Delta\sigma_c$ rate amounts to almost 1 kPa/yr at the ~9-km seismogenic depth. Where the tailings-induced stress changes are aligned with the background tectonic loading and slip on the WFZ, the tailings load would have been able to alter the time of eventual ruptures.

On the other hand, the activity of cluster *E* on the other side of the WVFZ remains puzzling (Hu & Bürgmann, 2020). Although two independent clusters are evident in the 1981-2018 catalog (e.g., Figs. 3e, k, and S6), the M5.7 event and its aftershocks suggest these two clusters are interconnected, possibly through slow slip (e.g., Xue et al., 2018) and/or pore pressure diffusion along the WFZ (e.g., Freed, 2005; Goebel & Brodsky, 2018). There could also be a direct pore-pressure effect from the overlying tailings pond and/or the aquifer system in the southeast graben. A delayed activation of aftershocks in cluster *E* by about one week may be a consequence of a permeable fault system allowing for pore pressure to diffuse along the fault zone over the course of about a week (Fig. 2c).

None of the clusters (Hu & Bürgmann, 2020) or the state-wide seismicity (Figs. S2-S5) represent clear annual periodicity as observed in other hydrologically driven seismotectonic settings. While Utah contains the largest inland body of saltwater in the Western Hemisphere, the Great Salt Lake and its tributary the Utah Lake, together with seasonally variant hydrological forcing from soil moisture and snow, we do not find statistically significant seasonal activity. This may be due to the spatio-temporally complex loads producing both failure-encouraging and discouraging stress changes on the Wasatch fault system, throughout the year. Improved seismicity catalogs and knowledge of fault geometries in the region are required to better understand such modulation.

We also make some qualitative comparisons of surface loads and declustered seismicity on a regional scale (Fig. 4). Historical big events (M>6) in Utah occurred in the early 1990s and middle 1930s when the lake level reached lows (Fig. 4c). Modern-day seismographic networks started from 1974 for this region (Wong et al., 1995). Intriguingly, an evident seismic quiescence in the middle 1980s and the following increasing number of earthquakes from the late 1980s to early 1990s coincide with peak water levels and rapidly declining levels, respectively. However, in the last two decades we see little correlation between multi-annual variations in lake levels and seismicity rates.

5. Concluding Remarks

The March 18, 2020 Magna earthquake and its aftershocks, as well as clusters of microseismicity during the past four decades, occurred just east of a mine tailings impoundment.

Our study demonstrates a correlation between substantial Coulomb stress changes in the seismic clusters and at the M5.7 hypocenter due to aggregate ore deposition since the 1900s; however, the sign and magnitude of the stress changes vary over short distances and with fault geometry. The tailings impoundment produces Coulomb stressing rates as high as ~1 kPa/yr at depths greater than 8 km, comparable to the background tectonic loading rates, which may decelerate or accelerate the recurrence interval by a few hundred years in this low strain-rate environment. Hydrological loads from the Great Salt Lake, Utah Lake, aquifer, soil moisture and snow generate largely seasonal and low-amplitude stress changes that produce no evident seasonal signature in local and regional earthquake catalogs and were at up to ~0.4 kPa at the time of the Magna earthquake. The shallow and localized anthropogenic loads may exert a more fundamental control than the regional hydrological sources on the seismicity in the SLC region. To improve our understanding of the connection between the manmade and natural surface loads and seismicity, we require better knowledge of the geometry of small and large faults, the magnitude and rate of tectonic stress, and the 3D elastic structure of the lithosphere. Interdisciplinary efforts exploring geotechnical, geophysical, geodetic, and seismic data and models are warranted for a better understanding of such mechanical interactions and appropriate mitigation measures.

Acknowledgement

We thank University of Utah Seismograph Stations (UUSS) for providing earthquake catalogs (https://quake.utah.edu/earthquake-information-products/earthquake-catalogs); Utah Automated Geographic Reference Center (AGRC) for providing the location of Quaternary faults (https://gis.utah.gov/data/geoscience/quaternary-faults/); U.S. Geological Survey (USGS)

for providing the Great Salt Lake levels (https://waterdata.usgs.gov/ut/nwis/uv/?site_no=10010000); Bureau of Reclamation for providing the Utah Lake levels (https://www.usbr.gov/rsvrWater/HistoricalApp.html); NOAA National Weather Service's National Operational Hydrologic Remote Sensing Center (NOHRSC) for providing the snow water equivalent estimates in the SNOw Data Assimilation System (SNODAS) (https://www.nohrsc.noaa.gov/archived_data/); NASA Goddard Earth Sciences Data and Information Services Center (GES DISC) for providing the soil moisture and snow water equivalent estimates for validation in North American Land Data Assimilation System (NLDAS) (https://disc.gsfc.nasa.gov/datasets/NLDAS_NOAH0125_M_002/summary?keywords=NLDAS); UVAVCO for providing GPS velocities for the eastern Basin-Range province (https://www.unavco.org/data/gps-gnss/gps-gnss.html); National Agriculture Imagery Program (NAIP) for providing the aerial imagery (https://datagateway.nrcs.usda.gov/GDGHome_DirectDownLoad.aspx). The Pylith code (Aagaard et al., 2013) is available at the Computational Infrastructure for Geodynamics (geodynamics.org/cig/software/pylith/).

References

1. Aagaard, B., Kientz, S., Knepley, M., Strand, L., & Williams, C. (2013). Pylith user manual: Version 2.1. 0. Davis, CA: Computational Infrastructure of Geodynamics.
2. Amos, C. B., Audet, P., Hammond, W. C., Bürgmann, R., Johanson, I. A., & Blewitt, G. (2014). Uplift and seismicity driven by groundwater depletion in central California, *Nature*, *509*, 483–486.

3. Ampuero, J.-P., Billant, J., Brenguier, F., Cavalié, O., Courboulex, F., Deschamps, A., Delouis, B., Grandin, R., Jolivet, R., Liang, C., Mordret, A., & Oral, E. (2020). The November 11 2019 Le Teil, France M5 earthquake: a triggered event in nuclear country. EGU General Assembly 2020, Online, 4–8 May 2020. https://doi.org/10.5194/egusphere-egu2020-18295
4. Argus, D. F., Fu, Y., & Landerer, F. W. (2014). Seasonal variation in total water storage in California inferred from GPS observations of vertical land motion. *Geophysical Research Letters*, *41*, 1971–1980.
5. Arabasz, W. J., Pechmann, J. C., & Brown, E. D. (1992). Observational seismology and the evaluation of earthquake hazards and risk in the Wasatch Front area, Utah, in W. W. Hays, and P. L. Gori (eds.), Assessment of Regional Earthquake Hazards and Risk Along the Wasatch Front, Utah. U.S. Geological Survey Professional Paper, p. D1-D36.
6. Bagge, M., Hampel, A., & Gold, R. D. (2019). Modeling the Holocene slip history of the Wasatch fault (Utah): Coseismic and postseismic Coulomb stress changes and implications for paleoseismicity and seismic hazard. *GSA Bulletin*, *131*(1–2), 43–57.
7. Bettinelli, P., Avouac, J.-P., Flouzat, M., Bollinger, L., Ramillien, G., Rajaure, S., & Sapkota, S. (2008). Seasonal variations of seismicity and geodetic strain in the Himalaya induced by surface hydrology. *Earth and Planetary Science Letters*, *266*, 332–344.
8. Bills, B. G., Currey, D. R., & Marshall, G. A. (1994). Viscosity estimates for the crust and upper mantle from patterns of lacustrine shoreline deformation in the Eastern Great Basin. *Journal of Geophysical Research: Solid Earth*, *99*, 22059–22086.

9. Bowman, S. D., & Arabasz, W. J. (2017). Utah Earthquakes (1850–2016) and Quaternary Faults. Utah Geological Survey Map 277. Available at https://ugspub.nr.utah.gov/publications/maps/m-277.pdf
10. Costain, J. K., & Bollinger, G. A. (2010). Review: Research Results in Hydroseismicity from 1987 to 2009. *Bulletin of the Seismological Society of America*, *100*(5A), 1841–1858.
11. Craig, T. J., Chanard, K., & Calais, E. (2017). Hydrologically-driven crustal stresses and seismicity in the New Madrid Seismic Zone. *Nature Communications*, *8*, 2143.
12. Chang, W.-L., Smith, R. B., Meertens, C. M., & Harris, R. A. (2006). Contemporary deformation of the Wasatch Fault, Utah, from GPS measurements with implications for interseismic fault behavior and earthquake hazard: Observations and kinematic analysis. *Journal of Geophysical Research: Solid Earth*, *111*.
13. DuRoss, C. B., & Lund, W. R. (2013). Sleeping giant—The earthquake threat facing Utah's Wasatch Front. Seismological Society of America 2013 Annual Meeting, Field Trip Guide, 20 p.
14. DuRoss, C. B., Personius, S. F., Crone, A. J., Olig, S. S., Hylland, M. D., Lund, W. R., & Schwartz, D. P. (2016). Fault segmentation: New concepts from the Wasatch Fault Zone, Utah, USA. *Journal of Geophysical Research: Solid Earth*, *121*, 1131–1157.
15. DuRoss, C. B., & Hylland, M. D. (2015). Synchronous ruptures along a major graben-forming fault system—Wasatch and West Valley fault zones, Utah, USA. *Bulletin of the Seismological Society of America*, *105*, 14–37.
16. Dziewonski, A. M., & Anderson, D. L. (1981). Preliminary reference Earth model. *Physics of the Earth and Planetary Interiors*, *25*(4), 297–356.

17. Ellsworth, W. (2013). Injection-Induced Earthquakes. *Science*, *341*.
18. Freed, A. M. (2005). Earthquake triggering by static, dynamic, and postseismic stress transfer. *Annual Review of Earth and Planetary Sciences*, *33*, 335–368.
19. Ge, S., Liu, M., Lu, N., Godt, J. W., & Luo, G. (2009). Did the Zipingpu reservoir trigger the 2008 Wenchuan earthquake? *Geophysical Research Letters*, *36*, L20315.
20. Gilbert, G. K. (1890). Lake Bonneville, U.S. Geol. Surv. Monogr., 1,438 pp.
21. Goebel, T. H. W., & Brodsky, E. E. (2018). The spatial footprint of injection wells in a global compilation of induced earthquake sequences. *Science*, *361*(6405), 899–904.
22. González, P., Tiampo, K., Palano, M., Cannavó, F., & Fernández, J. (2012). The 2011 Lorca earthquake slip distribution controlled by groundwater crustal unloading. *Nature Geoscience*, *5*, 821–825.
23. Gupta, H. K. (2002). A review of recent studies of triggered earthquakes by artificial water reservoirs with special emphasis on earthquakes in Koyna, India. *Earth-Science Reviews*, *58*(3–4), 279–310.
24. Gwynn, J. W. (1996). Commonly asked questions about Utah's Great Salt Lake and ancient Lake Bonneville. Utah Geological Survey, Public Information Series, 39, p 22.
25. Herring, T. A., Melbourne, T. I., Murray, M. H., Floyd, M. A., Szeliga, W. M., King, R. W., Phillips, D. A., Puskas, C. M., Santillan, M., & Wang, L. (2016). Plate Boundary Observatory and related networks: GPS data analysis methods and geodetic products. *Reviews of Geophysics*, *54*.
26. Herrmann, R. B., Benz, H., & Ammon, C. J. (2011). Monitoring the earthquake source process in North America. *Bulletin of the Seismological Society of America*, *101*, 2609–2625.

27. Hetzel, R., & Hampel, A. (2005). Slip rate variations on normal faults during glacial–interglacial changes in surface loads. *Nature*, *435*, 81–84.
28. Hu, X., & Bürgmann, R. (2020). Aquifer deformation and active faulting in Salt Lake Valley, Utah, USA. *Earth and Planetary Science Letters*, accepted. Preprint available at EarthArXiv https://eartharxiv.org/c7jex/
29. Hu, X., Oommen, T., Lu, Z., Wang, T., & Kim, J. W. (2017). Consolidation settlement of Salt Lake County tailings impoundment revealed by time-series InSAR observations from multiple radar satellites. *Remote Sensing of Environment*, *202*, 199–209.
30. Hu, X., Lu, Z., & Wang, T. (2018). Characterization of hydrogeological properties in Salt Lake Valley, Utah using InSAR. *Journal of Geophysical Research: Earth Surface*, *123*.
31. Johnson, C. W., Fu, Y., & Bürgmann, R. (2017). Seasonal water storage, stress modulation, and California seismicity. *Science*, *356*(6343), 1161–1164.
32. Johnson, C. W., Fu, Y., & Bürgmann, R. (2020). Hydrospheric modulation of stress and seismicity on shallow faults in southern Alaska. *Earth and Planetary Science Letters*, *530*, 115904.
33. Li, T., Cai, M. F., & Cai, M. (2007). A review of mining-induced seismicity in China. *International Journal of Rock Mechanics and Mining Sciences*, *44*(8), 1149–1171.
34. Mitchell, K. E., et al. (2004). The multi-institution North American Land Data Assimilation System (NLDAS): Utilizing multiple GCIP products and partners in a continental distributed hydrological modeling system. *Journal of Geophysical Research: Solid Earth*, *109*, D07S90.

35. National Operational Hydrologic Remote Sensing Center (NOHRSC) (2004). Snow Data Assimilation System (SNODAS) Data Products at NSIDC, Boulder, Colorado USA. National Snow and Ice Data Center.
36. Pang, G., Koper, K. D., Mesimeri, M., Pankow, K. L., Baker, B., Farrell, J., Holt, J., Hale, J. M., Roberson, P., Burlacu, R., Pechmann, J. C., Whidden, K., Holt, M., Allam, A., DuRoss, C. (2020). Evidence for a Listric Wasatch Fault From the 2020 Magna, Utah, Earthquake Sequence. Preprint. https://doi.org/10.1002/essoar.10503691.1
37. Pankow, K. L., Moore, J. R., Hale, J. M., Koper, K. D., Kubacki, T., Whidden, K. M., & McCarter, M. K. (2014). Massive landslide at Utah copper mine generates wealth of geophysical data. *GSA Today*, *24*(1).
38. Qian, Y., Chen, X., Luo, H., Wei, S., Wang, T., Zhang, Z., & Luo, X. (2019). An extremely shallow Mw4.1 thrust earthquake in the eastern Sichuan Basin (China) likely triggered by unloading during infrastructure construction. *Geophysical Research Letters*, *46*, 13,775.
39. Rio Tinto (2019). Tailings Impoundment. Avaiable at https://riotintokennecott.com/wp-content/uploads/2019/05/Tailings.pdf (accessed May 2020)
40. Rubinstein, J. L., & Mahani, A. B. (2015). Myths and facts on wastewater injection, hydraulic fracturing, enhanced oil recovery, and induced seismicity. *Seismological Research Letters*, *86*(4), 1060–1067.
41. Talwani, P. (1997). On the nature of reservoir-induced seismicity. *Pure and Applied Geophysics*, *150*, 473–492.
42. UUSS [@UUSSquake] (2020a). This conceptual model illustrates one possible scenario for the location of the M5.7 Magna earthquake and its aftershocks relative to the Wasatch

fault and associated faults. [Tweet]. Retrieved from https://twitter.com/UUSSquake/status/1243552563762360320

43. UUSS [@UUSSquake] (2020b). To the Science Community: Relocations of the aftershocks from March 18 through March 24 indicate that the Magna earthquake ruptured a west dipping fault, which is part of the Wasatch Fault system. The cross-section shows the location of the mainshock and aftershocks. [Tweet]. Retrieved from https://twitter.com/UUSSquake/status/1243257902170685440
44. Velasco, M. S., Bennett, R. A., Johnson, R. A., & Hreinsdottir, S. (2010). Subsurface fault geometries and crustal extension in the eastern Basin and Range province, western U.S. *Tectonophysics*, *488*, 131–142.
45. Verdecchia, A., Carena, S., Pace, B., & DuRoss, C. B. (2019). The effect of stress changes on time-dependent earthquake probabilities for the central Wasatch fault zone, Utah, USA. *Geophysical Journal International*, *219*(2), 1065–1081.
46. Wiemer, S. (2001). A software package to analyze seismicity: ZMAP. *Seismological Research Letters*, *72*(3), 373–382.
47. Wetzler, N., Shalev, E., Göbel, T., Amelung, F., Kurzon, I., Lyakhovsky, V., & Brodsky, E. E. (2019). Earthquake swarms triggered by groundwater extraction near the Dead Sea Fault. *Geophysical Research Letters*, *46*, 8056–8063.
48. Whidden, K. M., & Pankow, K. L. (2012). A Catalog of Regional Moment Tensors in Utah from 1998 to 2011. *Seismological Research Letters*, *83*(5).
49. Wong, I., Olig, S., Green, R., Moriwaki, Y., Abrahamson, N., Baures, D., Silva, W., Somerville, P., Davidson, D., Pilz, J., Dunne, B. (1995). Seismic hazard evaluation of the

Magna tailings impoundment. Environmental and Engineering Geology of the Wasatch Front Region, Utah Geological Association Publication 24, pp. 95-110.

50. Xue, L., Bürgmann, R., Shelly, D. R., Johnson, C. W., & Taira, T. (2018). Kinematics of the 2015 San Ramon, California earthquake swarm: Implications for fault zone structure and driving mechanisms. *Earth and Planetary Science Letters*, *489*, 135–144.
51. Xue, L., Johnson, C. W., Fu, Y., & Bürgmann, R. (2020). Seasonal seismicity in the western branch of the East African Rift System. *Geophysical Research Letters*, *47*, e2019GL085882.

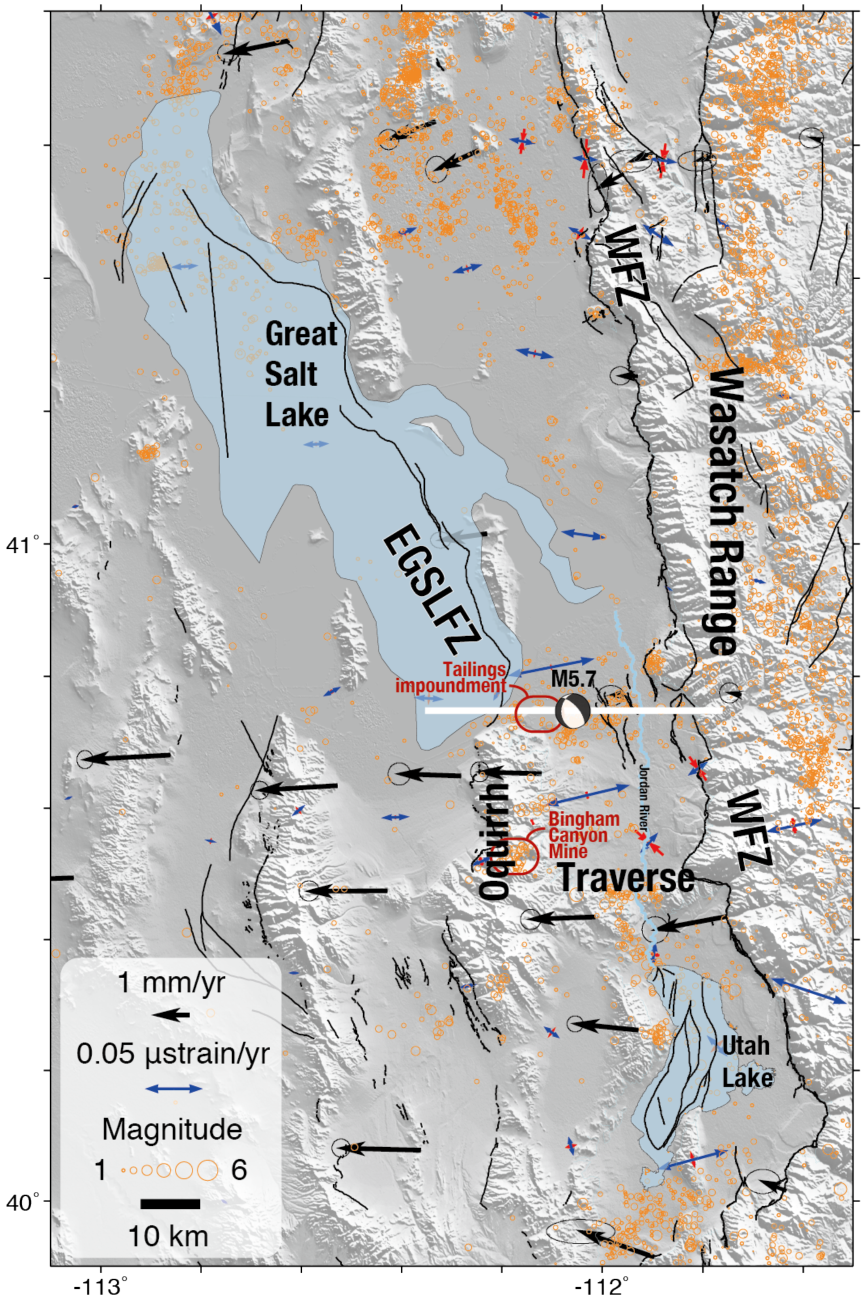

Fig. 1. Map of north-central Utah along the eastern edge of the Basin and Range province. Black arrows, tipped with 95% confidence ellipses, show the GPS horizontal velocities in the stable North America reference frame (Herring et al., 2016). Blue and red arrow pairs show the extensional and contractional principal strain-rate axes. Orange circles show the contemporary 1981-2018 earthquake catalog (M>0.82) archived at the University of Utah Seismograph Stations (UUSS) and their size represents the magnitude. Black lines show Quaternary faults. The Wasatch Fault Zone (WFZ) extends along the frontal Wasatch Range. The East Great Salt Lake Fault Zone (EGSLFZ) underlies the Great Salt Lake. The Jordan River (blue line) connects the Great Salt Lake and Utah Lake. The EW trending white line shows the profile used in Fig. 4.

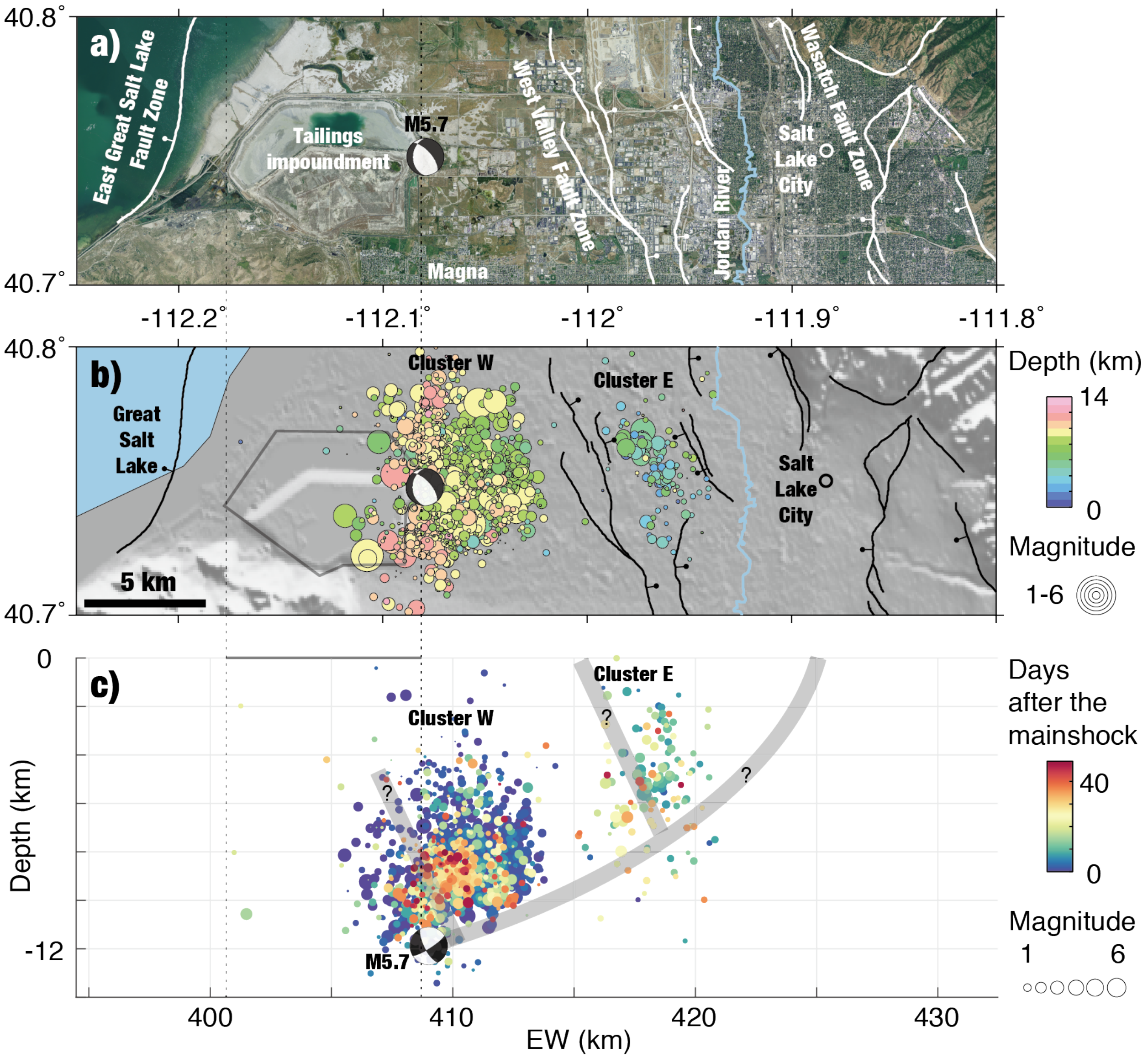

Fig. 2. M5.7 Magna earthquake sequence. (a) Aerial imagery of the study area. (b) The M5.7 Magna earthquake and its aftershocks. The white lines in (a) and black lines in (b) show the west-dipping Wasatch Fault Zone (WFZ) and East Great Salt Lake Fault Zone, and the mostly east-dipping West Valley Fault Zone (WVFZ) (DuRoss and Hylland, 2015). (c) Side view of M5.7 event and its aftershocks. The size of the circles represents the magnitude and the color denotes the number of days after the March 18, 2020 mainshock at a depth of 11.9 km. The focal mechanism of the main shock comes from USGS. The two vertical dashed lines indicate the bounds of the tailing impoundment. The thick gray lines give a schematic view of the inferred listric structure of the WFZ (Velasco et al., 2010), the conjugate WVFZ, and an unconfirmed east-dipping fault plane, modified from Wong et al. (1995), DuRoss & Lund (2013), and UUSS (2020a).

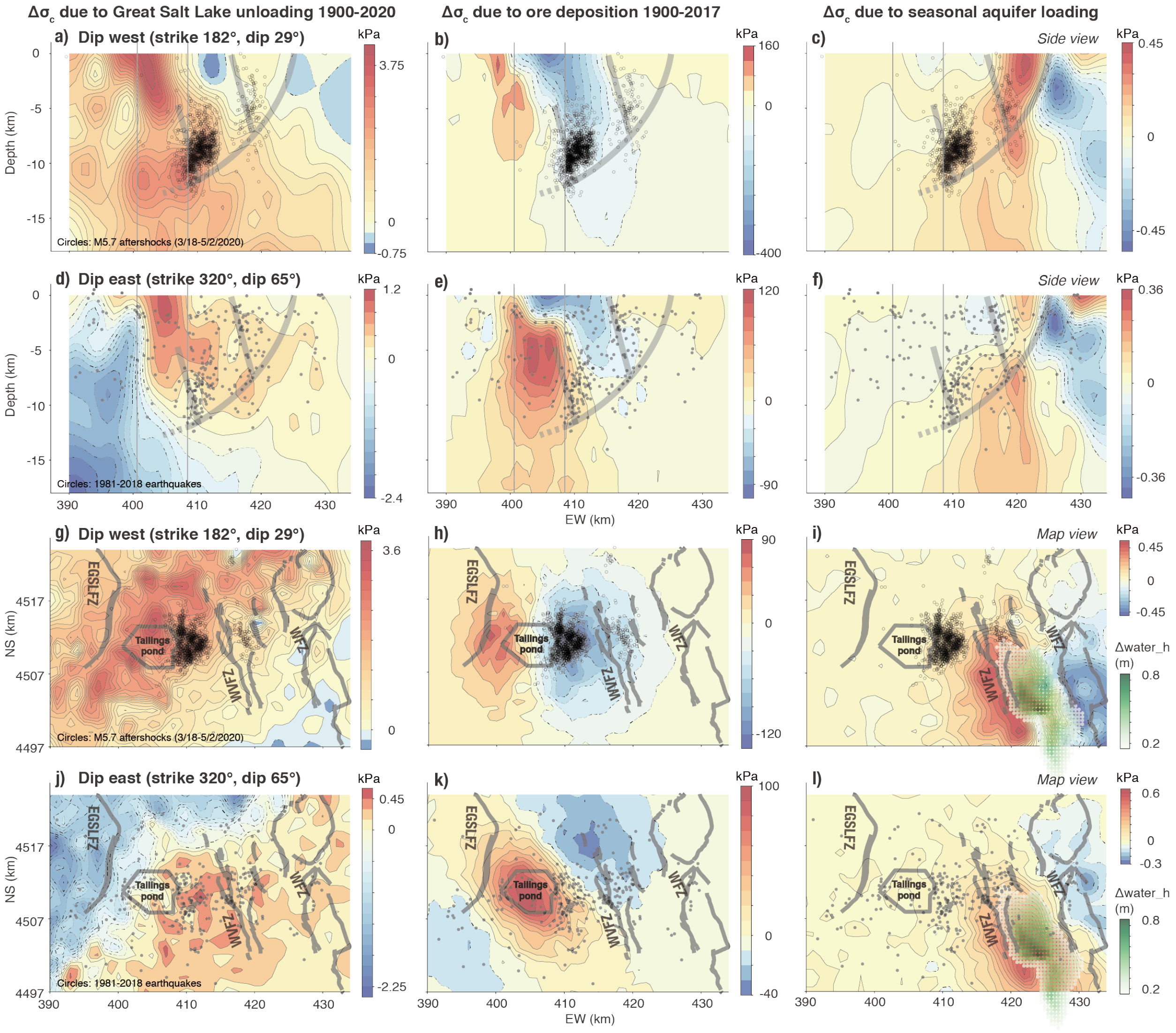

Fig. 3. Cross sections of the Coulomb stress changes $\Delta\sigma_c$ associated with long-term Great Salt Lake and tailings loads, as well as seasonal aquifer surface load changes. (a) to (f) show the EW cross section results along the white line in Fig. 1. Vertical lines show the edges of the tailings pond. Bold gray lines show a schematic view of the inferred faults (Fig. 1c). (g) to (l) show the map view results of the stress field at a depth of 9 km. Thick lines show the fault traces. Polygons outline the tailings impoundment. First column (a, d, g, j) shows $\Delta\sigma_c$ due to the Great Salt Lake level decrease since 1900 (USGS). Second column (b, e, h, k) shows $\Delta\sigma_c$ due to the ore deposition at the tailings impoundment from 1905 to 2017. Third column (c, f, i, l) shows $\Delta\sigma_c$ due to the seasonal aquifer water change (greenish dots in panels h and k; Hu & Bürgmann, 2020). The first and third rows consider a receiver fault with strike of 182° and dip of 29° (to the west) in a pure normal faulting regime; circles show the M5.7 Magna earthquake aftershock locations. The second and fourth rows consider a receiver fault with a strike of 320° and dip of 65° (to the east) in a pure normal faulting regime; circles show the 1981-2018 earthquake locations.

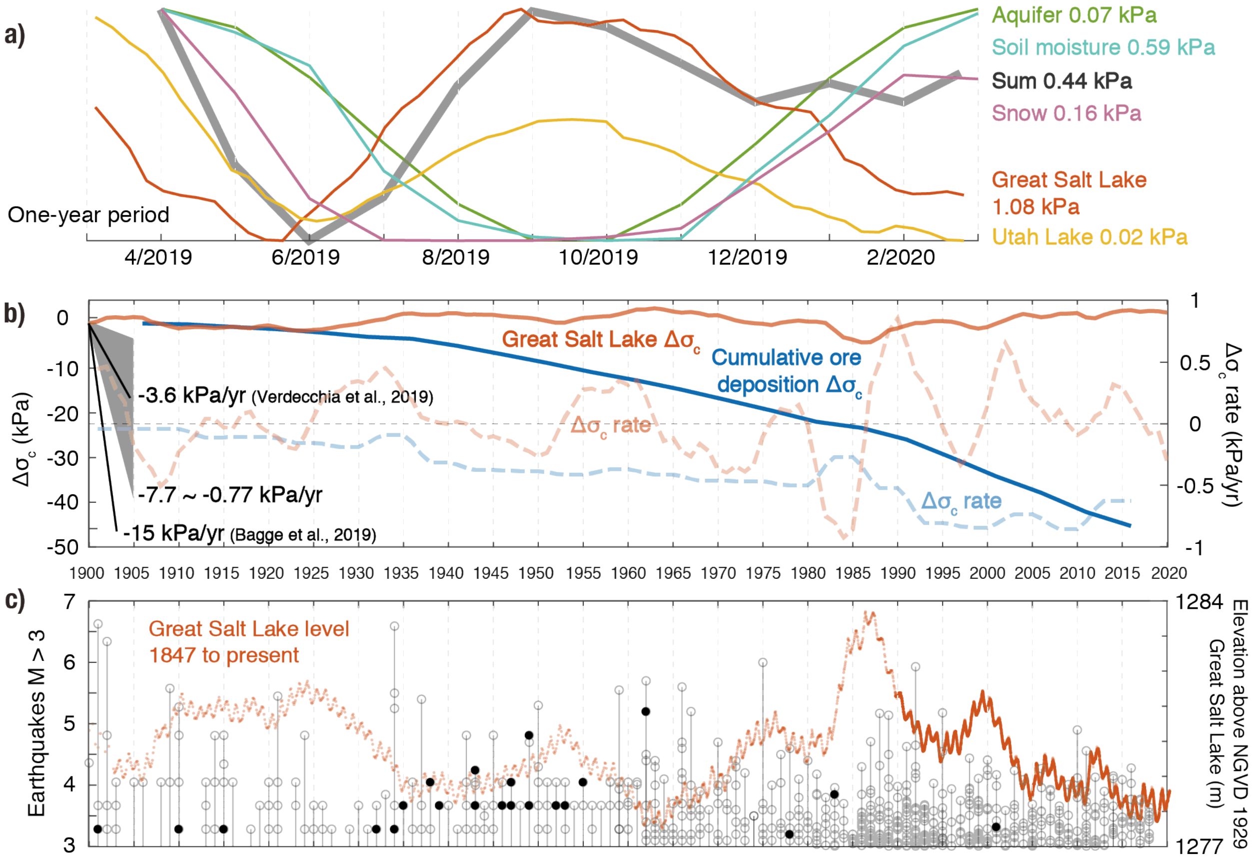

Fig. 4. Time-series Coulomb stress changes $\Delta\sigma_c$ at the hypocenter of the 2020 M5.7 Magna earthquake considering a strike of 182° and 29° west dipping geometry. (a) Seasonal $\Delta\sigma_c$ due to different hydrological loading sources during a one-year period (3/2019 to 2/2020) preceding the Magna earthquake. The seasonal amplitudes of stress changes from each loading source are denoted. (b) Long-term evolution of $\Delta\sigma_c$ and annual rates of $\Delta\sigma_c$ due to ore deposition (blue solid and dashed lines) and Great Salt Lake load (orange solid and dashed lines), from 1900 to 2020. Black lines represent the reported tectonic loading rates (Bagge et al., 2019; Verdecchia et al., 2019) and our back-of-the-envelope estimate. (c) The stem plot shows M>3 earthquakes across Utah (Lat. 36.75° to 42.50° N, Long. 108.75° to 114.25° W) in open circles and those in the Salt Lake City region (Lat. 40.6° to 40.9° N, Long. 111.8° to 112.25° W) in solid circles. Orange curve shows the Great Salt Lake level.